This is a preprint, the final version is subject to change, of the American Mineralogist (MSA)
Cite as Authors (Year) Title. American Mineralogist, in press.
DOI: https://doi.org/10.2138/am-2020-7266

REVISION 1

Morin-type transition in 5C pyrrhotite

C R S Haines[1*], G I Lampronti[1], W T Klooster[2], S J Coles[2], S E Dutton[3], and M A Carpenter[1]

[1]*Department of Earth Sciences, University of Cambridge, Cambridge, UK*

[2]*UK National Crystallographic Service, Chemistry, Faculty of Natural and Environmental Sciences, University of Southampton, SO17 1BJ, UK*

[3]*Department of Physics, University of Cambridge, Cambridge, UK*

Abstract

We report the discovery of a low temperature spin-flop transition in 5C pyrrhotite at ~155 K that is similar to those seen in hematite at 260 K and FeS (troilite) at 440 K. The 5C crystal was produced by annealing a 4C pyrrhotite crystal at 875 K, to produce a change in the vacancy-ordering scheme that developed during cooling. The 5C structure is confirmed by single crystal x-ray diffraction and the stoichiometry and homogeneity by electron microprobe and SEM BSE mapping. RUS, heat capacity and magnetisation measurements from room temperature down to 2 K are reported. The transition is marked by a steep change in elastic properties at the transition temperature, a peak in the heat capacity and weak anomalies in measurements of magnetisation. Magnetic hysteresis loops and comparison with the magnetic properties of 4C pyrrhotite suggest that the transition involves a change in orientation of moments between two different antiferromagnetic structures, perpendicular to the crystallographic *c*-axis at high temperatures and parallel to the crystallographic *c*-axis at low temperatures. The proposed structures are

This is a preprint, the final version is subject to change, of the American Mineralogist (MSA)
Cite as Authors (Year) Title. American Mineralogist, in press.
DOI: https://doi.org/10.2138/am-2020-7266

consistent with a group theoretical treatment that also predicts a first order transition between the magnetic structures.

This is a preprint, the final version is subject to change, of the American Mineralogist (MSA)
Cite as Authors (Year) Title. American Mineralogist, in press.
DOI: https://doi.org/10.2138/am-2020-7266

I. INTRODUCTION

The pyrrhotite system comprises a number of related structures having compositions $Fe_{1-x}S$ where $0 < x < 0.125$. The best known of these structures are troilite (FeS) and 4C pyrrhotite (Fe_7S_8). 4C is so called because it is a superstructure with a 4 cell repeat along the *c*-axis with respect to the parent NiAs structure (Bertaut 1953; Powell 2004). Other commensurate superstructures have been reported as 3C (Fleet 1971, Nakano et al 1979), 5C (de Villiers et al 2009, Elliot 2010, Liles and de Villiers 2012) and 6C (Koto et al 1975, de Villiers and Liles 2010), while some are incommensurate (Nakazawa and Morimoto 1971, Morimoto et al 1975, Yamamoto and Nakazawa 1982, Izaola et al 2007). Ferrimagnetic pyrrhotite (4C) is an important carrier of magnetic remanence on earth and possibly also on Mars (e.g. Martin-Hernandez et. al 2008; Rochette et. al 2005), but 4C structures are not unique and the other superstructure types have different structure/property relationships which are much less well known. The key issue in relation to the magnetic structures are how vacancies order on the cation sites as the stoichiometry changes and how the distribution of vacancies then controls the magnetic structures.

By adopting a group theoretical approach, Haines et al. (2019a) have shown that the commensurate superstructures of pyrrhotite, which have different Fe/vacancy ordering schemes, are all likely to undergo a magnetically driven spin reorientation transition with accompanying small distortions of the crystal lattice at low temperatures. The prediction for the case of 5C pyrrhotite is for an abrupt spin-flop transition similar to the Morin transition in hematite. The present work focuses on the magnetic and elastic properties of a natural 4C crystal that transformed unexpectedly to 5C crystal after being heated above its concomitant vacancy ordering and Néel temperature of 595 K. We report a newly identified magnetic transition at ~155 K in the 5C crystal and propose that it is a spin-flop transition between two

antiferromagnetic structures, with an origin that is closely related to that of the magnetic transitions already known in FeS at 440 K and 4C Fe_7S_8 at 35 K.

In general, 5C pyrrhotite is found to have a composition close to Fe_9S_{10}. However, Pósfai et. al. (2000) reported a 5C polytype with composition Fe_7S_8. Kontny et. al. (2000) also presented some x-ray diffraction and magnetisation measurements on multiphase samples, suggesting the possibility of pyrrhotite with a 5C structure having the stoichiometry close to the Fe_7S_8 that is usually associated with the 4C structure. De Villiers et al. (2009) proposed space group number 63 *Cmce* (formerly *Cmca*) as the correct crystallographic space group at room temperature. Elliot (2010) had claimed $P2_1/c$ for the room temperature structure. Liles and de Villiers (2012) subsequently proposed $P2_1$ for the structure at both room temperature and 120 K. There do not appear to have been any studies of the magnetic structure.

In this work, we first establish the stoichiometry of the sample through electron microprobe analysis before going on to present a structural solution in the space group 63 *Cmce* based on single crystal diffraction data collected on a single crystal sample of 5C pyrrhotite at room temperature. We then present heat capacity, DC magnetisation and resonant ultrasound spectroscopy (RUS) measurements on a second single crystal over the range 2-300 K.

II. SAMPLE PREPARATION

The single crystal sample of pyrrhotite used in this study was cut from a cm-sized crystal in the mineral collection of the South Australia Museum that had originated from a mine in Mexico. Samples from the same parent crystal have been described in Haines et al (2019c). At the start, it was nearly in the shape of a rectangular parallelepiped with two pairs of parallel faces 1.7 mm and 1.5 mm apart and a third pair of non-parallel faces separated by between 1 mm and 1.5mm. The first experiment was to collect RUS spectra through the temperature interval 10 -

295 K to confirm that it was 4C pyrrhotite with a Besnus transition (Besnus and Meyer 1964) at ~35 K (see Haines et al. 2019b).

After removal from the RUS instrument, the crystal was heated slowly to 875 K in flowing argon, with an oxygen trap, over four and a half days before cooling it back to room temperature over three days. The sample was held between two alumina rods. The heating and cooling rates through the 595 K transition were 2.2 K/hour. As a consequence of this treatment, the crystal acquired a thin oxide layer that was removed mechanically, and also broke into two pieces. The larger piece had a mass of 9.1±0.1 mg and was used for heat capacity, magnetisation and RUS measurements. On completion of these measurements, the larger piece was mounted and polished for chemical analysis. The smaller piece weighed 2.2±0.1 mg and was broken up for the single crystal diffraction measurements.

III. ELECTRON MICROPROBE ANALYSIS

Chemical analysis on the larger piece was carried out using a Cameca SX100 electron microprobe in the Department of Earth Sciences, University of Cambridge (instrumental conditions: 20 keV, 10 nA, 1μm beam diameter). With respect to 10 sulphur atoms, the average of 20 analyses gave the number of Fe atoms as 9.21±0.05. Co, Cu, Mn, Ni and Zn were measured for, but all were below the detection limit on all of the 20 analysis spots. We highlight here that this shows a significant change in stoichiometry from the parent crystal described in Haines et al. (2019c) in which electron microprobe analysis revealed a homogeneous and pure 4C crystal of stoichiometry 7.00(6) Fe atoms per 8 sulphur atoms. We suggest that this change of stoichiometry is due to the loss of sulphur from the crystal rather than the addition of iron for which no source or mechanism is present. To check for zoning or inhomogeneity in the stoichiometry of the crystal a scanning electron microscope back-scattered electron (SEM-BSE) analysis map of nearly the whole surface of the same piece used for the electron microprobe

analysis was collected. The SEM-BSE map showed no sign of any chemical inhomogeneity above the level of detection. We therefore conclude that the transformation from stoichiometry $Fe_{7.00(6)}S_8$ to $Fe_{9.21(5)}S_{10}$ is complete and homogeneous. The images are included as supplemental information (SI 2020).

IV. SINGLE CRYSTAL X-RAY DIFFRACTION

The single crystal used for X-ray diffraction was black and plate-shaped, with dimensions ~0.080 x 0.040 x 0.020 mm^3. It was mounted on a MITIGEN holder in perfluoroether oil on a Rigaku FRE+ diffractometer equipped with VHF Varimax confocal mirrors and an AFC12 goniometer and HyPix 6000HE detector. The temperature was 293 ± 2 K during scans of 0.5° per frame for 1.3 s with Mo K radiation (Rotating-anode X-ray tube, 40 kV, 30 mA). The total number of runs and images was based on the strategy calculation from the program CrysAlisPro (Rigaku, V1.171.39.46, 2018). The maximum resolution achieved was at 27.478° (0.77 Å). Cell parameters were retrieved using the CrysAlisPro (Rigaku, V1.171.39.46, 2018) software and refined using CrysAlisPro (Rigaku, V1.171.39.46, 2018) on 5787 reflections, 22% of the observed reflections. Data reduction, scaling and absorption corrections were performed using CrysAlisPro (Rigaku, V1.171.39.46, 2018). The final completeness is 99.7 % out to 25° in Θ. A multi-scan absorption correction was performed using CrysAlisPro 1.171.39.46 (Rigaku Oxford Diffraction, 2018) using spherical harmonics as implemented in SCALE3 ABSPACK. The absorption coefficient of this material is 13.664 mm^{-1} at this wavelength (= 0.711Å) and the minimum and maximum transmissions are 0.522 and 1.000.

Figure 1 shows a section of the (0*kl*) plane of the diffraction pattern, with 5 superlattice reflections clearly visible along the $c^*(k_z)$ of the parent NiAs cell. We looked for evidence of incommensuration by initially indexing the pattern with the NiAs unit cell and then using an

incommensurate k-vector to describe the remaining peaks. The k-vector which describes the pattern has components of 0.500(3) along the planar hexagonal axes and 0.204(6) perpendicular to the ab-plane of the parent structure. This is therefore commensurate within experimental uncertainty.

The structural solution and subsequent refinement were undertaken using the SHELXS program (Sheldrick 1997), proceeding with 9 Fe and 8 S atomic positions. Neutral scattering factors were used for all atoms. The appropriate 3-individual twin matrix describing a 120° rotation along the c axis was introduced in the first stages of the refinement; since the three individual fractions were found to be all close to 33%, this step was necessary to take the discrepancy factor $R1$ below 0.2. Individual occupancy factors for the Fe atoms were refined with an overall isotropic thermal parameter to detect the partially vacant sites. The Fe sites that refined to occupancies close to 1.0 were then fixed at unity, and the thermal displacement parameters were then refined independently. Lastly, the ADPs were refined anisotropically, together with the occupancies of the four partially vacant Fe atoms. Because of an unreasonably prolate ADP for the atom at (0,0,0) Fe9 the thermal displacement parameters were restrained to be similar to those of the neighbour Fe sites. We here highlight that this is not the same position found to be vacant in the structural refinement performed by De Villiers et al. (2009), corresponding to Fe4 in our model. Details of the structural solutions are given in the accompanying cif file.

The refinement converged with a discrepancy factor $R1 = 0.0485$ for 1675 observed reflections and $R1 = 0.0604$ for all 2084 measured reflections and 120 parameters. The goodness of fit parameter was $S = 1.476$ and $wR2$ was 0.3431. No extinction correction parameter was used as it was found to converge to zero. The largest residual electron density amounted to 1.32 e/Å. Interestingly, the structural model reported by De Villiers et al. (2009) also differs in the way the Fe planes stack along the [001] direction (see Figure 2).

The composition, calculated from the refinement of the structure, is $Fe_{9.22(1)}S_{10}$, in excellent agreement with the results of the electron microprobe analysis. Details of the refinement and the comparison to that of De Villiers et al. (2009) are given in Table 1. A cif file containing detailed information about data collection and structural refinement is supplied separately.

V. HEAT CAPACITY

Heat capacity measurements were carried out in a Quantum Design PPMS. The 9.1mg sample was fixed to the measurement platform of the heat capacity puck with Apiezon N grease. The puck (plus grease) was measured through the temperature interval 2-300 K with and without the sample to determine the background contribution needed to obtain the heat capacity of the sample alone. At low temperatures the heat capacity of the sample was larger than the background but at temperatures above ~30K the background was larger.

Figure 3a shows a peak in the heat capacity of the crystal near 155 K. Broad features at 215 K and 280 K are artefacts due to the Apiezon grease. A closer view of the peak (Fig. 3b) reveals it to be at 154 K with an apparent onset temperature of ~147 K and a tail up to ~157 K. Repeat measurements in a field of 9 T applied parallel to the [100] direction of the crystal (*H*//*a* of the NiAs cell) yielded a peak at 148 K (Fig. 3b). The shape of the peak was unchanged, but the transition had clearly been shifted down in temperature by ~6 K. There is no evidence in the data for the Besnus transition at 35 K, which confirms that the crystal had fully transformed from the 4C structure. The peak is asymmetric. There is a shoulder on the low temperature side

171 suggesting that there are two contributions to the peak. This is somewhat similar to the heat
172 capacity anomaly recently observed in 4C pyrrhotite (Haines *et al.* 2019b).
173
174 **VI. MAGNETISATION**
175 Magnetisation was measured using a Quantum Design MPMS. Zero field cooled (ZFC) data
176 were collected by cooling the crystal in zero applied field to 2 K before applying a 10 mT field
177 ($H//a$) and measuring the moment in a continuous heating sweep up to 300 K at 3K/min. Field
178 cooled (FC) data were collected by cooling the crystal to 2 K in an applied field of 5 T before
179 removing the 5T field and applying a 10 mT field ($H//a$) during measurements of the moment in
180 a continuous heating sweep up to 300 K at 3K/min. There are two distinct features observable in
181 both the ZFC and FC magnetisation curves, at ~120 and ~155 K. The feature at ~155 K cannot
182 be explained by any obvious impurity and matches up well with the transition seen in the heat
183 capacity of the 5C crystal. The feature at ~120 K is almost certainly from the Verwey transition
184 of magnetite, revealing the presence of a small amount of magnetite as an impurity phase. This is
185 most likely remaining from incomplete removal of the thin oxidised layer, following the heat
186 treatment at 875 K. The same crystal was used for both magnetisation and heat capacity
187 measurements, and the lack of any anomalies in the heat capacity at ~120 K supports the
188 conclusion that the proportion of magnetite was very small.
189 In order to put the absolute values of magnetisation in context, results for the 5C crystal and
190 for a 4C crystal cut from the parent crystal temperature are compared in Figure 4b. 4C pyrrhotite
191 is ferrimagnetic, due to an uncompensated moment arising from the fact that one in eight Fe sites
192 are vacant. The measured moment of the 4C crystal at room temperature is a factor of ~100
193 larger than that of the 5C crystal, suggesting that the magnetic ground state of 5C pyrrhotite is a
194 fully compensated antiferromagnet. Furthermore, this puts an upper limit on the amount of 4C

pyrrhotite remaining in the sample of approximately 1%. In the ZFC data the step-like feature at 155 K takes place between 148 K and 155 K, with a midpoint of 152 K. The start stop and mid-points of the step in the FC data are the same, though there is a small kink at the mid-point that is not observed in the ZFC data.

Figure 5a contains hysteresis (*M*-*H*) loops measured between +7 and –7 T at two temperatures well above and two temperatures well below the magnetic transition. The values of *M* never exceed ~2 Am^2/kg and are smaller at all fields by a factor of at least ten in comparison with the 4C structure (Powell et. al 2004; Charilou et. al 2015). They also show no indication of saturation at any temperature, consistent with antiferromagnetic structures. Above the transition, the magnetisation at 7 T (1.8 Am^2/kg) is more than 4 times larger than it is below the transition (0.4 Am^2/kg) at the same field. Below 150 K, [100] is a relatively hard direction, but becomes relatively soft above ~150 K. The difference remains marked even at 140 and 160 K, but there is a metamagnetic transition at 150 K from the low temperature magnetic structure, at low fields, to the high temperature structure at high fields (Fig. 5b). This is permissive of a first order spin-flop transition between two antiferromagnetic structures that have their moments aligned in the plane perpendicular to the *c*-axis above the transition point and parallel to the *c*-axis below it. In this scenario, small openings of the curves at low fields (Fig. 5c) and the small hysteresis seen in the magnetisation curves at all temperatures are attributed to the magnetite impurity identified on the basis of the magnetic anomaly at ~120 K (Fig. 3a). In addition, the (near) saturation moment of these two impurities (at a field of 1.5 T) would limit their presence in the sample to similar values. If the entire signal at 300 K and 1.5 T were attributed to magnetite (this is around 0.5 Am^2/kg) this would equate to 46 μg of magnetite or 0.5% of the total mass, using a value of 90 Am^2/kg for saturation magnetisation of magnetite (Hunt et al. 2103 and references therein). In a

similar way we can constrain the 4C pyrrhotite to be less than 2.5% of the total mass (using 20 Am^2/kg as the value of the magnetisation from Hunt et al. (1995) and Haines et al (2019b).

VII. RESONANT ULTRASOUND SPECTROSCOPY

Details of the instrument used to collect RUS data at low temperatures have been given elsewhere (McKnight et. al 2007). The sample sits lightly between two piezoelectric transducers in the RUS head, which is attached to the end of a stick and lowered into an Orange helium flow cryostat. In the present study, resonance spectra were collected in two automated cooling and heating sequences with steps of 30 K on cooling from room temperature to 10 K, and of between 1K and 10K on heating from 10 K to 295 K. A settle time of 1200s was included to allow for thermal equilibration at each set point. Individual spectra contained 65,000 data points in the frequency range 100 kHz – 2 MHz, with a driving voltage of 25 V. One sequence was for a different piece of the original large 4C crystal and the second was for the 9.1 mg fragment of the 5C crystal. Analysis of elastic and anelastic properties was undertaken by fitting selected peaks with an asymmetric Lorentzian function to give peak frequency, f, and width at half-maximum height, Δf. The natural resonances of a mm sized sample involve primarily shearing motions and the variations of f^2 therefore reflect variations of different combinations of predominantly shear elastic constants, in this case of the single crystal. Acoustic dissipation is expressed in terms of the inverse mechanical quality factor, Q^{-1}, which, in a RUS experiment is usually specified as $\Delta f/f$.

Figure 6 contains a stack of spectra from the heating sequence of the 5C crystal. The y-axis is amplitude, but the spectra have been offset in proportion to the temperatures at which they were collected. The axis has then been relabelled as temperature in order to allow ready visualisation of the principal features of the elastic behaviour. All the resonances show the same pattern of

reducing frequency (elastic softening) as the transition point is approached from above, followed by abrupt increases (elastic stiffening) at the expected transition temperature of ~155 K. In other words, all the shear elastic constants of the crystal evolve in more or less the same manner. Blue curves are fits to individual peaks, and Figure 7a shows the variations of f^2 and Q^{-1} for a peak near 650 kHz. With falling temperature there is a trend of elastic softening by a few percent towards the transition point, followed by ~10% stiffening in a narrow temperature interval between 150 and 160 K. This temperature interval corresponds almost exactly with the temperature interval over which the anomaly in heat capacity extends (Fig. 3). The peaks generally remain quite sharp at all temperatures, with values of Q^{-1} in the vicinity of $2x10^{-3}$ apart perhaps from a slight increase in the vicinity of the transition point. The variation of f^2 normalised to the room temperature value for three different peaks is shown in Figure 7b. Whilst the overall temperature dependence is similar the peaks behave slightly differently, as would be expected for a single crystal sample in which each resonance has a distinct contribution from the different elastic constants.

Variations of f^2 and Q^{-1} data from fits to a resonance peak near 620 kHz in spectra collected from the piece of original the 4C crystal are shown in Figure 7c. The crystal was cut from the same original sample as the piece that was converted to 5C. There are very obvious differences from the variations in elastic and anelastic properties that accompany the magnetic transition shown in Figure 7. In particular, softening by a few % with falling temperature is associated with a peak in Q^{-1} at ~270 K. This turns into a trend of gradual stiffening followed by steep softening ahead of the Besnus transition, which is marked by a minimum at ~36 K. f^2 values then recover steeply and there is a distinct peak in Q^{-1} immediately below the transition. The maximum change in f^2 at the frequency of this resonance, ~620 kHz, is ~6%. Changes in elastic and

anelastic properties accompanying the Besnus transition in 4C pyrrhotite are described in detail elsewhere (Haines et al 2019b).

VIII. DISCUSSION AND CONCLUSIONS

We have shown that 4C pyrrhotite can be transformed to 5C by annealing above the concomitant Néel and vacancy ordering temperature. On the basis of single crystal x-ray diffraction at room temperature we confirm that a model in space group *Cmce* can successfully explain the diffraction data. The low temperature structure has previously been refined successfully using a model in space group $P2_1$ by Liles and deVilliers (2012). The Besnus transition is no longer observed and a new Morin-like spin-flop transition occurs at ~155 K instead. The magnetic properties of the 5C crystal are incompatible with impurities of 4C pyrrhotite or magnetite above the level of 1%. In addition, the heat capacity anomalies characteristic of the low temperature magnetic phase transitions in these two minerals were not observed. The 4C crystal from which the piece used in this study was cut showed no impurities above the level of detection in either powder XRD or electron microprobe measurements (Haines et al. 2019b). Therefore, it is difficult to imagine any impurity other than the magnetite formed at the surface or 'untransformed' 4C pyrrhotite. We have carried out electron microprobe analysis on the 5C crystal and the sample is monophase with a high degree of homogeneity. The impurity levels are on the border of detectability. The stoichiometry is homogeneous and works out to be $Fe_{9.2}S_{10}$ in good agreement with the single crystal refinement.

The most significant structural difference in comparison with the 4C structure is the change in vacancy ordering scheme which develops during cooling. Without specifying the ordering in detail, it is possible to assess the changes in structure and properties from the perspective of symmetry. If the reference structure at high temperatures is taken to be that of NiAs in space

group $P6_3/mmc$, the order parameter which gives rise to the 5C superstructure is most likely to have the symmetry of the active representation U1(1/2,0,1/5) (Haines et al 2019a). A likely candidate for the magnetic order parameter has the symmetry of irreducible representation $m\Gamma_5^+$. The list of possible magnetic space groups that can result from this combination includes the previously reported crystallographic space groups *Cmce*, $P2_1/c$ and $P2_1$ (Haines et. al 2019a). New magnetic and elasticity data have been interpreted here on the basis that 5C pyrrhotite is antiferromagnetic and that the magnetic transition at ~155 K is from one antiferromagnetic structure to another. In all of the reported space groups the moments can be aligned either in the plane perpendicular to the crystallographic *c*-axis of the parent or parallel to the *c*-axis. Across the $Fe_{1-x}S$ phase diagram (Schwarz and Vaughan 1972) the 590 K transition is to a state in which the moments are in the plane perpendicular to the crystallographic *c*-axis. The low temperature spin-flop transition observed in troilite and the low temperature evolution of 4C pyrrhotite involve a rotation of the moments towards the *c*-axis.

Haines et. al (2019a) predicted that the magnetic transition in 5C would be an abrupt spin-flop transition. This is because for none of the experimentally reported structures is it possible to have distortions which allow both $m\Gamma_4^+$ and $m\Gamma_5^+$ to have non-zero values. In other words, the moments are strictly confined to either the plane perpendicular to the *c*-axis or to the direction parallel to the *c*-axis. *Cmce* was reported for a crystal at room temperature with the $P2_1$ structure being solved using data collected at 120 K. These two structures do not have a group-subgroup relationship so that a *Cmce* – $P2_1$ transition is necessarily first order.

The spin-flop transition in 5C pyrrhotite is significantly different from the Besnus transition in 4C pyrrhotite, as is seen clearly in differences between the two sets of elastic and anelastic data in Figure 7. As a function of temperature, the spin-flop transition is characterised by a steep increase in all the shear elastic constants over a narrow temperature interval, consistent with first

order character. The low temperature structure is stiffer than the high temperature structure and has the same level of acoustic loss. In contrast, the Besnus transition occurs over a wider temperature interval, consistent with a second order transition between magnetic structures that do have a group-subgroup relationship. There is also a distinct peak in the acoustic loss that could relate to the development of a ferroelastic microstructure. Thus, the transition in the 5C crystal appears to be closely analogous to the magnetic transition to that seen in FeS at 440 K, which involves the same change in orientation of moments (Harihara and Murakami 1958, Andresen 1960, Sparks et. al 1960 and1962, Andresen et. al 1967, Horwood et al 1976).

This combination of symmetry analysis and experimental data on the magnetoelastic behaviour shows that 5C pyrrhotite fits well into the wider picture for the diverse structures suggested for the system $Fe_{1-x}S$ by Haines et al (2019a). The stable antiferromagnetic/ferromagnetic structure which appears across the solid solution at ~590 K has moments aligned perpendicular to the crystallographic *c*-axis. At transition temperatures which reduce from ~440 K with increasing concentration of vacancies, this gives way to another magnetic structure in which the preferred orientation of the moments is 90° away from the *c*-axis. Details of the precise magnetic structure and possibilities for thermodynamically continuous pathways between the two magnetic states then depend on details of the vacancy ordering at different stoichiometries, as expressed in terms of order parameters with irreducible representations of the form U(1/2,0,1/x) where *x* is 3, 4, 5, 6 or irrational, corresponding to the 3C, 4C, 5C, 6C and incommensurate phases of pyrrhotite. All these phases, apart from 3C, are expected to show one magnetic transition below room temperature. In 3C pyrrhotite the transition is expected to be above room temperature.

This is a preprint, the final version is subject to change, of the American Mineralogist (MSA)
Cite as Authors (Year) Title. American Mineralogist, in press.
DOI: https://doi.org/10.2138/am-2020-7266

IX. IMPLICATIONS

The discovery of a low temperature spin-flop transition in the 5C superstructure of pyrrhotite must be seen within the context of the whole $Fe_{1-x}S$ family. In this work we have shown that the behaviour of the 5C superstructure is consistent with a comprehensive group theoretical framework described in Haines *et al.* (2019a). The result fits with the 3C superstructure being ferrimagnetic at room temperature and, if the crystallographic space group of $P3_121$ (Nakano *et al*. 1979; Keller-Besrest *et al.* 1983) is correct, with the magnetic moments aligned parallel to the *c*-axis. A low temperature spin-reorientation transition like the Besnus transition must also be expected in the 6C superstructure. Thus, it seems that the spin flop transitions are all closely related and fundamentally due to the same underlying thermodynamic driving force.

An additional consideration relates to the fact that the 5C crystal studied in this work was the result of thermally cycling a 4C crystal through the concomitant vacancy ordering and ferrimagnetic ordering temperature, at 595 K, and then up to 875 K before cooling back to room temperature. To our knowledge, this is the first time that 5C pyrrhotite has been synthesised in this way.

Finally, our improved understanding of the nature of the vacancy ordering and related magnetic structures in the $Fe_{1-x}S$ system means that an understanding of the microscopic mechanisms may now be within reach for an important group of mineral sulphides. Further experiments and calculations should focus on the changes in electronic structure behind the changing magnetic anisotropy and its dependence on temperature, pressure and vacancy order.

ACKNOWLEDGMENTS

The authors acknowledge funding from the Leverhulme Foundation, grant number RPG2016-298. Heat capacity and DC magnetic measurements were carried out using the Advanced

Materials Characterisation Suite, funded by EPSRC Strategic Equipment Grant EP/M000524/1. RUS facilities in Cambridge were funded by grants to MAC from the Natural Environment Research Council of Great Britain (grant nos. NE/B505738/1 and NE/F17081/1) and from the Engineering and Physical Sciences Research Council (grant no. EP/I036079/1).

References

Andresen, A. F., Hofman-Bang, N., Bak, T. A., Varde, E. & Westin, G. (1960). Acta Chemica Scandinavica, 14, 919–926.

Andresen, A. F., Torbo, P., Ostlund, E., Bloom, G. & Hagen, G. (1967). Acta Chemica Scandinavica, 21, 2841–2848.

Bertaut, E. F. (1953). Acta Crystallographica, 6, 557-561

Besnus, M. J. & Meyer, A. J. P. (1964) Proceedings of the International Conference on Magnetism Nottingham 507-511

Charilaou, M., Kind, J., Koulialias, D., Weidler, P. G., Mensing, C., Löffler, J. F. & Gehring. A. U. (2015). Journal of Applied Physics, 118 083903

CrysAlisPro Software System, Rigaku Oxford Diffraction, (2018).

De Villiers, J. P. R. & Liles, D. C. & Becker, M. (2009). American Mineralogist, 94(10), 1405-1410.

De Villiers, J. P. R. & Liles, D. C. (2010). American Mineralogist, 95(1), 148-152.

Elliot, A. D. (2010). Acta Crystallographica Section B, 66(3), 271-279.

Fleet, M. E. (1971). Acta Crystallographica Section B, 27(10), 1864-1867.

Haines, C. R. S., Howard, C. J., Harrison, R. J. and Carpenter, M. A. (2019a) Acta Crystallographica Section B 75, 1208–1224

Haines, C. R. S., Volk, M., Dutton, S. E. and Carpenter, M. A. (2019b) *in preparation*

Haines, C. R. S., Lampronti, G. I.. and Carpenter, M. A. (2019c) *in preparation*

Horwood, J. L., Townsend, M. G. & Webster, A. H. (1976) Journal of Solid State Chemistry 17 17-42.

Hunt, C. P., Moskowitz, B. M. and Banerjee, S. K. (2013). Magnetic Properties of Rocks and Minerals. In Rock Physics & Phase Relations, T. J. Ahrens (Ed.). doi:10.1029/RF003p0189

Keller-Besrest, F., Collin, G. & Comes, R. (1983). *Acta Crystallographica Section B* **39**, 296-303.

Kontny, A., De Wall, H., Sharp, T., & Posfai, M. (2000). The American Mineralogist, 85(10), 1416-1427.

Koto, K., Morimoto, N., & Gyobu, A. (1975). Acta Crystallographica Section B, 31(12), 2759-2764.

Liles, D. C. & De Villiers, J. P. R. (2012). American Mineralogist, 97(2), 257-261.

Martín-Hernández, F., Dekkers, M., Bominaar-Silkens, I., & Maan, J. (2008). Geophysical Journal International, 174(1), 42-54.

Mcknight, R., Carpenter, M., Darling, T., Buckley, A., & Taylor, P. (2007). American Mineralogist, 92(10), 1665-1672.

Morimoto, N., Gyobu, A, Tsukuma, K, & Koto, K. (1975). The American Mineralogist., 60(3-4), 240-248.

Nakano, A., Tokonami, M. & Morimoto, N. (1979). Acta Crystallographica Section B, 35(3), 722–724.

Nakazawa, H. & Morimoto, N. (1971). Material Research Bulletin, 6 345-358.

Posfai, M., Sharp, T., & Kontny, A. (2000). The American Mineralogist, 85(10), 1406-1415.

Powell, A., Vaqueiro, P., Knight, K., Chapon, L. & Sanchez, R. (2004). Physical Review B, 70(1).

Rochette, P., Gattacceca, J., Chevrier, V., Hoffmann, V., Lorand, J., Funaki, M., & Hochleitner, R. (2005). Meteoritics & Planetary Science, 40(4), 529-540.

Schwarz, E. J. & Vaughan, D. J., (1972). Magnetic Phase Relations of Pyrrhotite. Journal of Geomagnetism and Geoelectricity. 24. 441-458. DOI:10.5636/jgg.24.441.

Sheldrick, G. M. (1997). shelxl97 and shelxs97. University of Göttingen, Germany.

Sheldrick, G.M., Acta Crystallographica Section C (2015), C27, 3-8.

Sparks, J. T., Mead, W., Kirschbaum, A. J. & Marshall, W. (1960). Journal of Applied Physics, 31(5), S356–S357.

Sparks, J. T., Mead, W. & Komoto, T. (1962) Journal of the Physical Society of Japan 17(Suppl. B-I) 249-252.

Yamamoto, A. & Nakazawa, H. (1982). Acta Crystallographica Section A, 38(1), 79–86.

Figure captions

Figure 1. Part of the (*0kl*) precession image of the room temperature single crystal X-ray diffraction pattern, showing the five-fold superlattice reflections of the 5C structure. The data has been reduced using the cell from the *Cmce* structure and the peaks are labelled with the (*hkl*) of the *Cmce* structure. The direction of the b^* and c^* are given in red on the left. The unit cell of the *Cmce* structure is shown by the grey grid. The projection of the hexagonal parent cell onto the *Cmce* (0*kl*) plane is shown in blue. The five-fold modulation in the *l* direction can be seen and the peaks characteristic of this are labelled with their (*hkl*) values.

Figure 2. Structural model of pyrrhotite 5C viewed along [100] from this work (top) and from de Villiers et al. (2009) (bottom). Color code: yellow = S sites; brown = Fe sites (partial occupancy is shown by half-grey half-brown); pink = partially Ni replaced Fe site (De Villiers et al., 2009); blue = vacant metal site from De Villiers et al. (2009) (see main text for details).

Figure 3. (a) Heat capacity of 5C crystal measured between 2 and 300 K in zero field, showing the magnetic transition near 155 K. Anomalies at ~215 and ~280 K are artefacts. (b) Higher resolution view of the peak at 154 K in zero field, which shifts to 148 K when measured in a 9 T field (*H*//*a*).

436 Figure 4. Magnetisation, *M*, of 5C crystal. (a) ZFC and FC data, measured in a field of 10 mT
437 (*H*//*a*). The anomaly at ~120 K is due to the presence of a small amount of magnetite (labelled
438 as T_V for the Verwey transition) as impurity phase. The previously unknown transition is
439 labelled as T_x. (b) Comparison with ZFC data for 4C and 5 C crystals (*H*//*a*), showing a
440 difference in magnetisation of a factor of ~100.
441
442 Figure 5. (a) Field and temperature dependence of the magnetisation of the 5C sample. The
443 field was applied parallel to the [100] direction of the parent NiAs structure unit cell (*H*//*a*). The
444 structure at 200 and 300 K has marked differences in magnetic anisotropy from the structure at 5
445 and 100 K. Neither show any indication of saturation at high fields. (b) Field and temperature
446 dependence of magnetisation of the 5C structure close to the magnetic transition at ~155 K
447 (*H*//*a*). (c) Close in view of the low field region from (b), showing slight opening of the loops
448 that is attributed to the presence of a small amount of magnetite.
449
450 Figure 6. RUS spectra collected from the 9.1 mg piece of the 5C crystal in a heating sequence
451 from 10 to 295 K. The y-axis should be amplitude in volts, but the spectra have been offset in
452 proportion to the temperatures at which they were collected and the axis relabelled as
453 temperature. There is an abrupt change in frequencies of all the individual resonance peaks at the
454 expected transition temperature, ~155 K. Fits to selected peaks are shown in blue.
455
456 Figure 7. (a) Temperature dependence of f^2 and Q^{-1} for the single crystal of 5C pyrrhotite
457 from fitting of the resonance peak near 650 kHz and (b) f^2 for three resonance peaks at 660 kHz,
458 780 kHz and 840 kHz normalised to the value at room temperature. (c) Temperature dependence
459 of f^2 and Q^{-1} for a single resonance with frequency near 620 kHz from a 4C pyrrhotite crystal cut

from the same original sample as was used to produce the 5C crystal. The Besnus transition is marked by a minimum if f^2 at ~36 K. Crosses = Q^{-1}, right axis; filled circles = f^2, left axis.

Tables

465 Table 1. Crystal data and structure refinement details for 5C pyrrhotite.

	This work	*De Villiers et al. (2009)*
Empirical formula	$Fe_{9.22(1)}S_{10}$	$Fe_{8.79}Ni_{0.118}S_{10}$
Formula weight	6682.51	6588.86
Temperature (ºK)	293(2)	293(2)
Wavelength (Å)	0.71073	0.71073
Space group	*Cmce* (formerly *Cmca*)	*Cmce* (formerly *Cmca*)
Unit cell dimensions	a = 6.890(2) Å	a = 6.893(3) Å
	b = 11.9436(4) Å	b = 11.939(3) Å
	c = 28.7916(10) Å	c = 28.635(15) Å
	α = 90º	α = 90º
	β = 90º	β = 90º
	γ = 90º	γ = 90º
Volume	2371.36(13) $Å^3$	2356.4(15) $Å^3$
Z, Calculated Density	8, 4.689 g/cm^3	8, 4.643 g/cm^3
Absorption coefficient	12.681	12.516
F(000)	3358	3154
Crystal size	0.08x 0.04 x 0.02 mm^3	0.14 x 0.06 x 0.03 mm^3
θ range for data collection	2.12-31.82º	2.85-26.34º
Limiting indices	$-9 \le h \le 9$, $-16 \le k \le 15$, $-40 \le l \le 42$	$-8 \le h \le 7$, $-8 \le k \le 14$, $-33 \le l \le 29$
Reflections collected/unique	29278/2084 [$R(int)$ = 0.0322]	6041/1264 [$R(int)$ = 0.0322]
Completeness to θ = 25.00	99.7%	99.2%
Refinement method	Full-matrix least-squares on F^2	Full-matrix least-squares on F^2
Data / restraints / parameters	2084 / 1 / 120	1264 / 0 / 109
Goodness-of-fit on F^2	1.477	1.225
Final R indices [I > 2θ(I)]	$R1$ = 0.0485, $wR2$ = 0.3231	$R1$ = 0.0716, $wR2$ = 0.1513
R indices (all data)	$R1$ = 0.0604, $wR2$ = 0.3431	$R1$ = 0.0937, $wR2$ = 0.1627
Extinctions coefficient	-	0.00003(2)
largest diff. peak and deepest hole	1.445 and -1.346 $e^- \cdot Å^{-3}$	1.533 and -2.125 $e^- \cdot Å^{-3}$

466

Figure 1

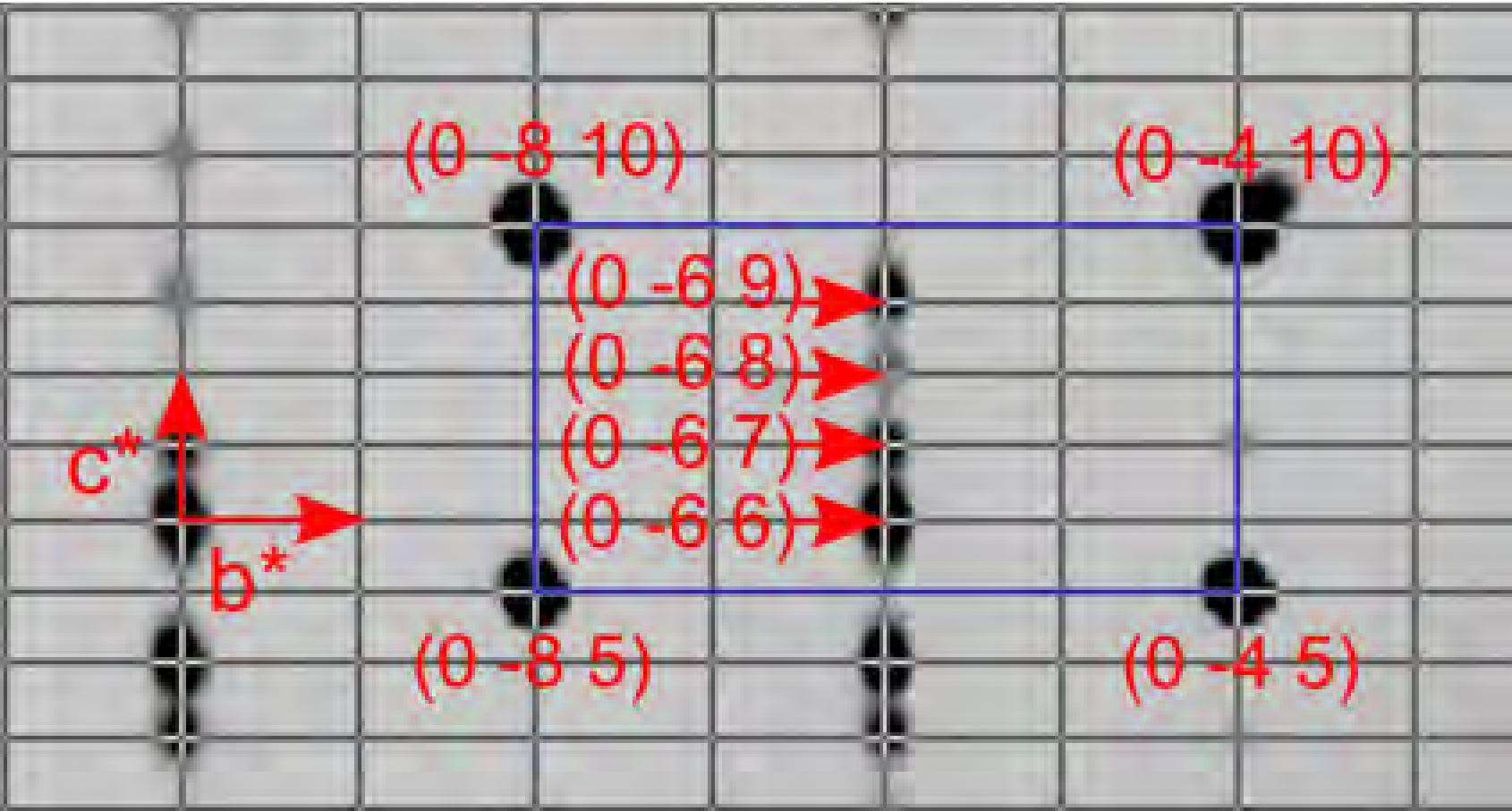

Figure 2

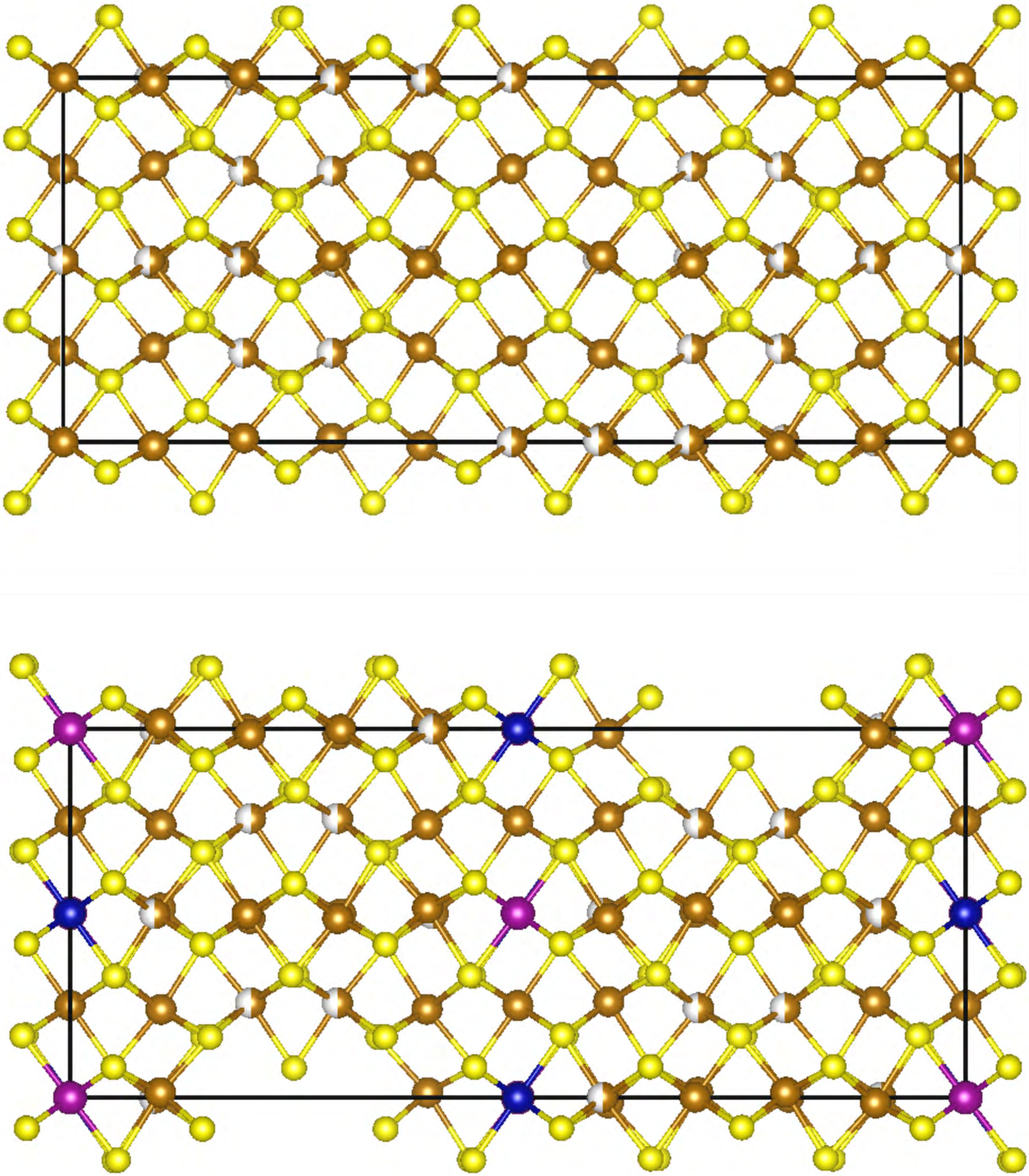

Figure 3a

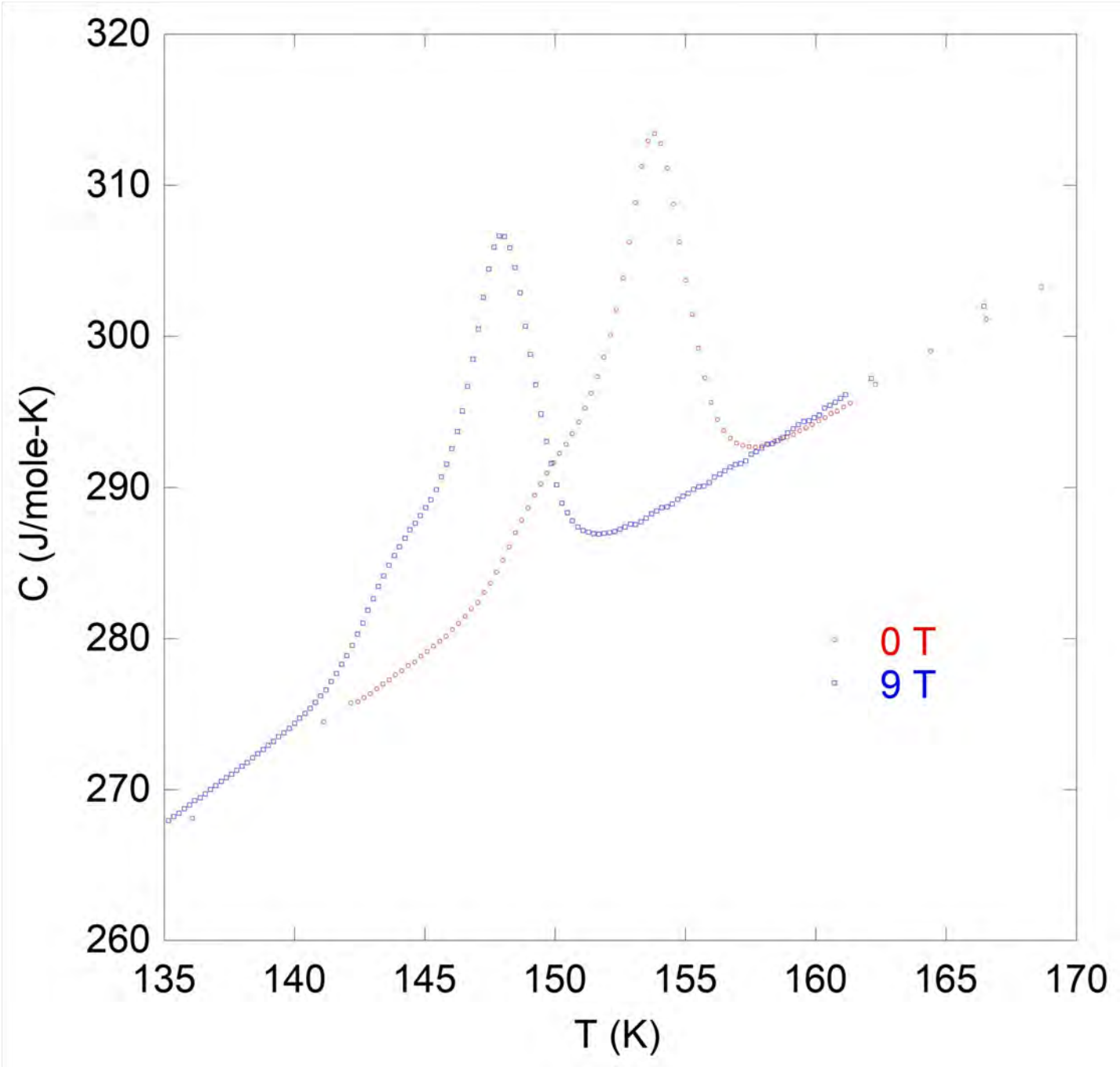
320
310
300
290
280
270
260
C (J/mole-K)
135
140
145
150
155
160
165
170
T (K)
0 T
9 T

a)

Figure 3b

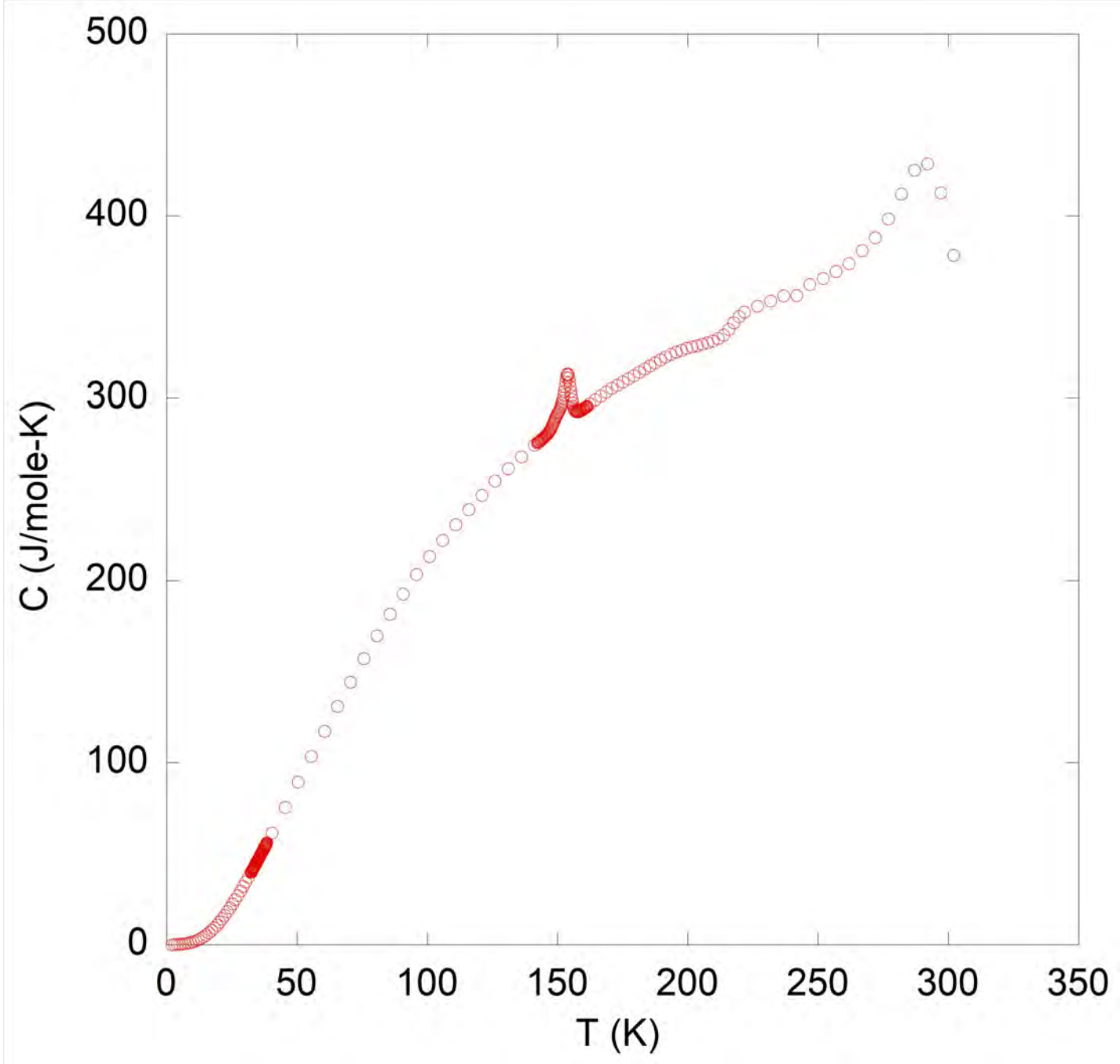

b)

Figure 4a

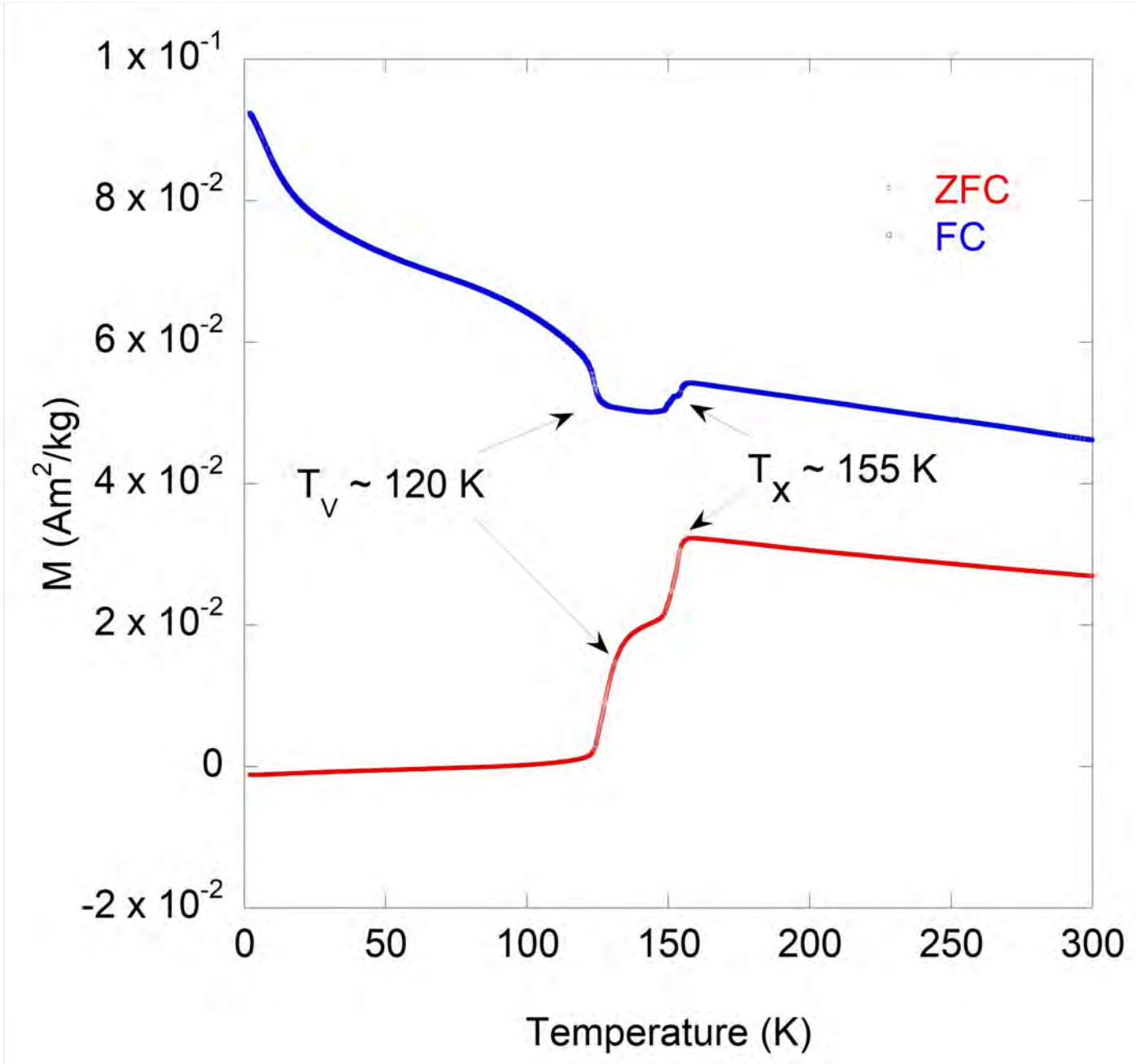
1 x 10-1
8 x 10-2
6 x 10-2
4 x 10-2
2 x 10-2
0
-2 x 10-2
M (Am2/kg)
ZFC
FC
TV ~ 120 K
Tx ~ 155 K
0
50
100
150
200
250
300
Temperature (K)

a)

Figure 4b

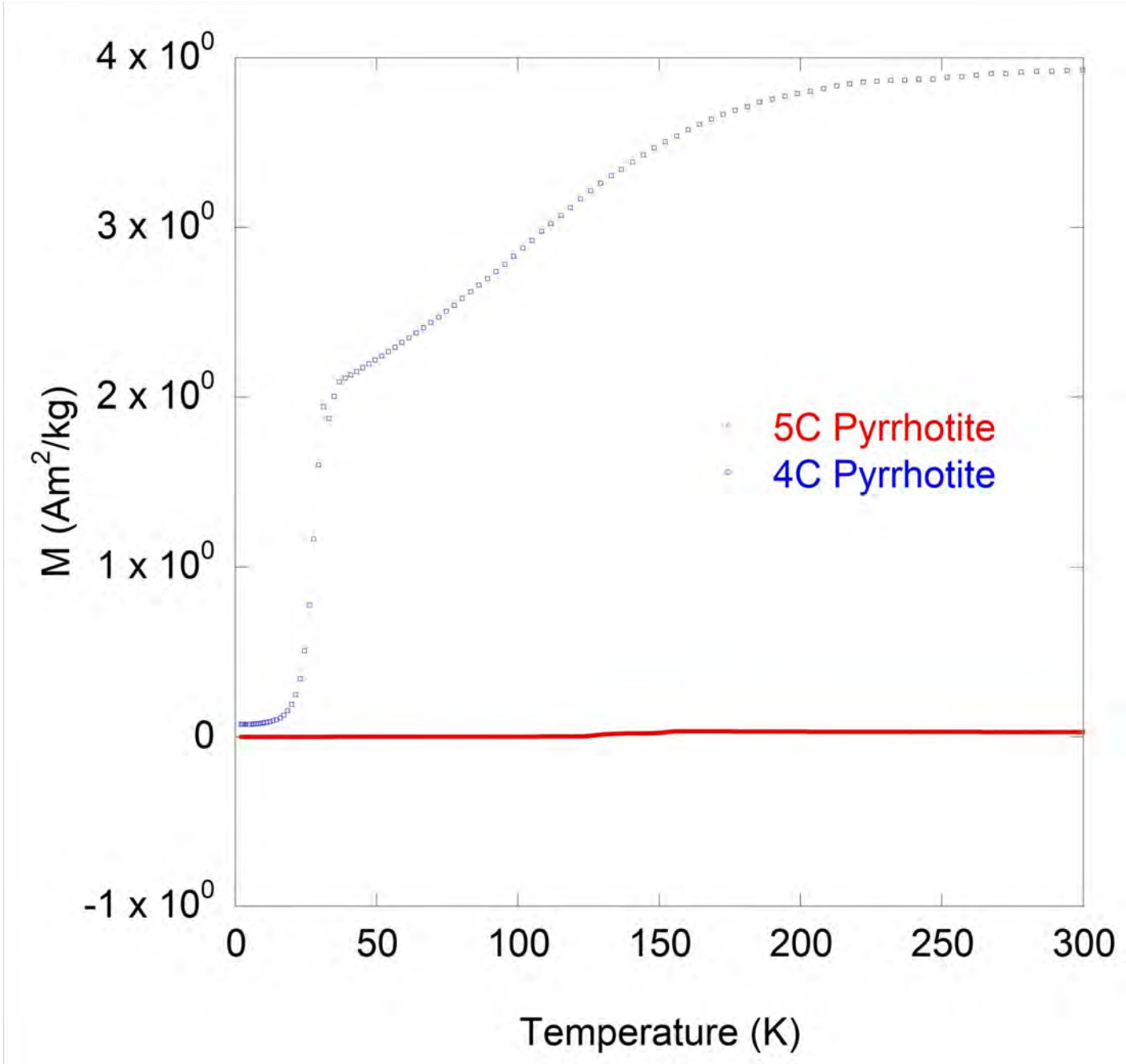
4 x 10^0
3 x 10^0
2 x 10^0
1 x 10^0
0
-1 x 10^0
M (Am^2/kg)
0
50
100
150
200
250
300
Temperature (K)
5C Pyrrhotite
4C Pyrrhotite

b)

Figure 5a

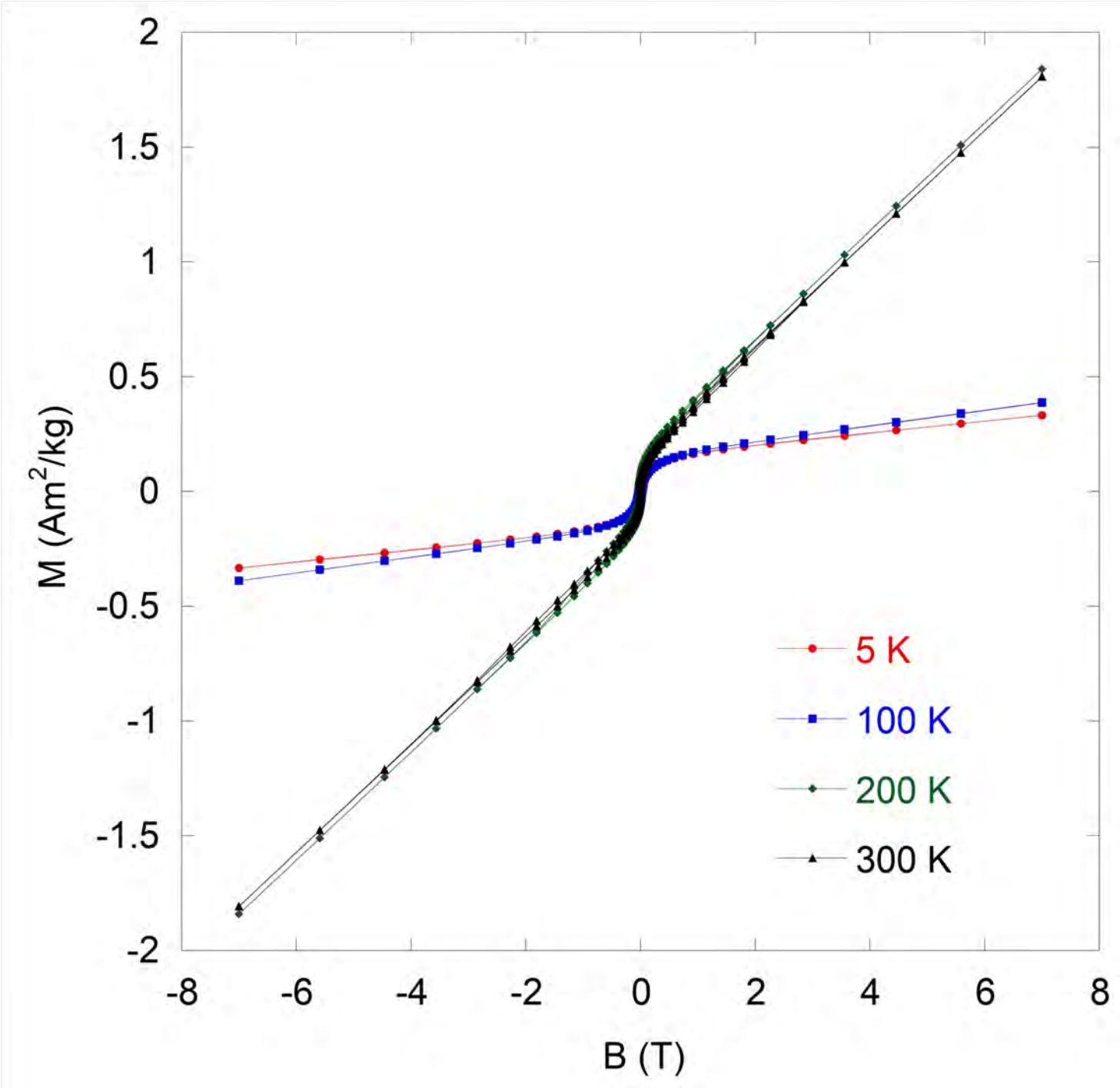

a)

Figure 5b

b)

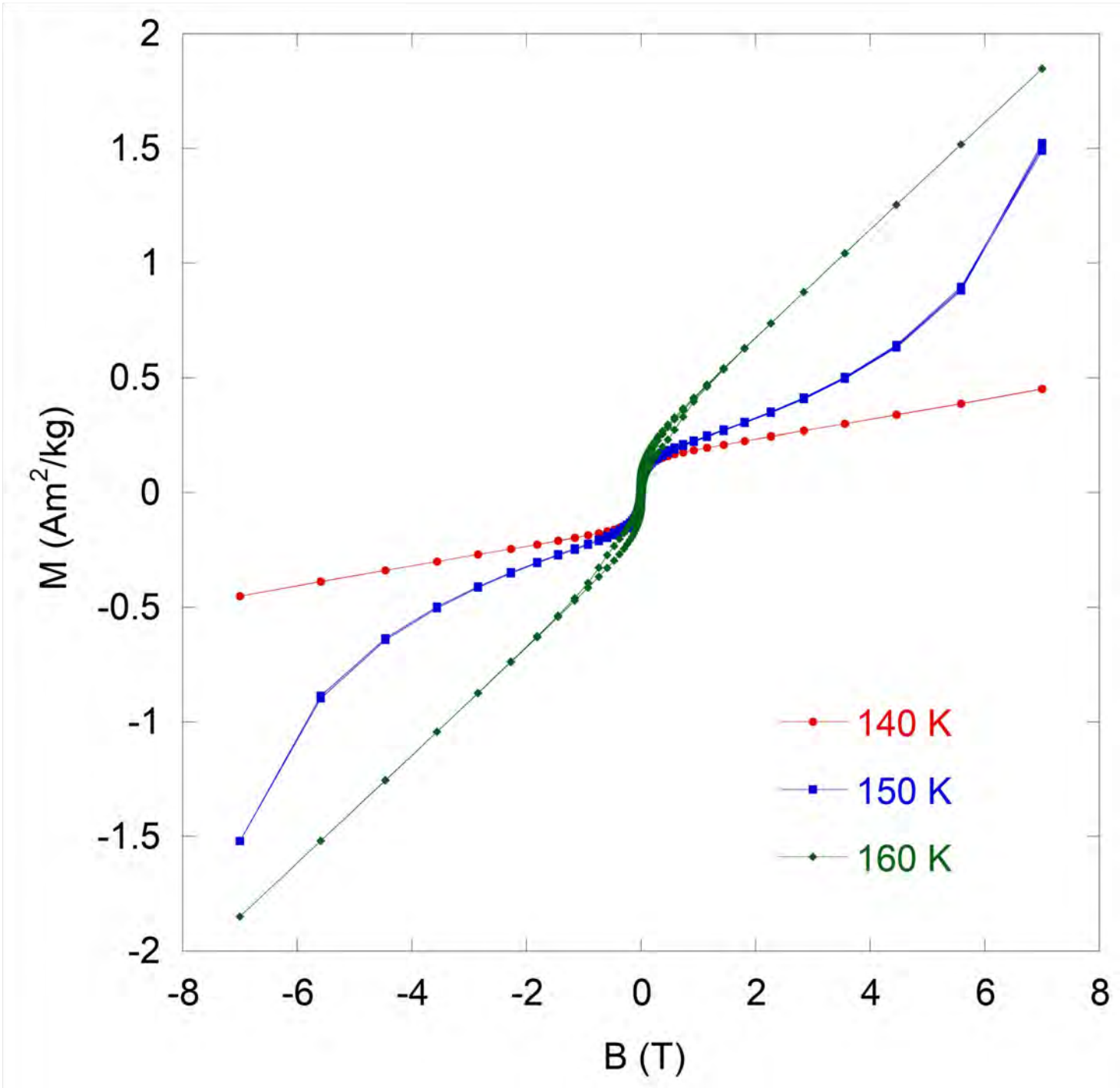

Figure 5c

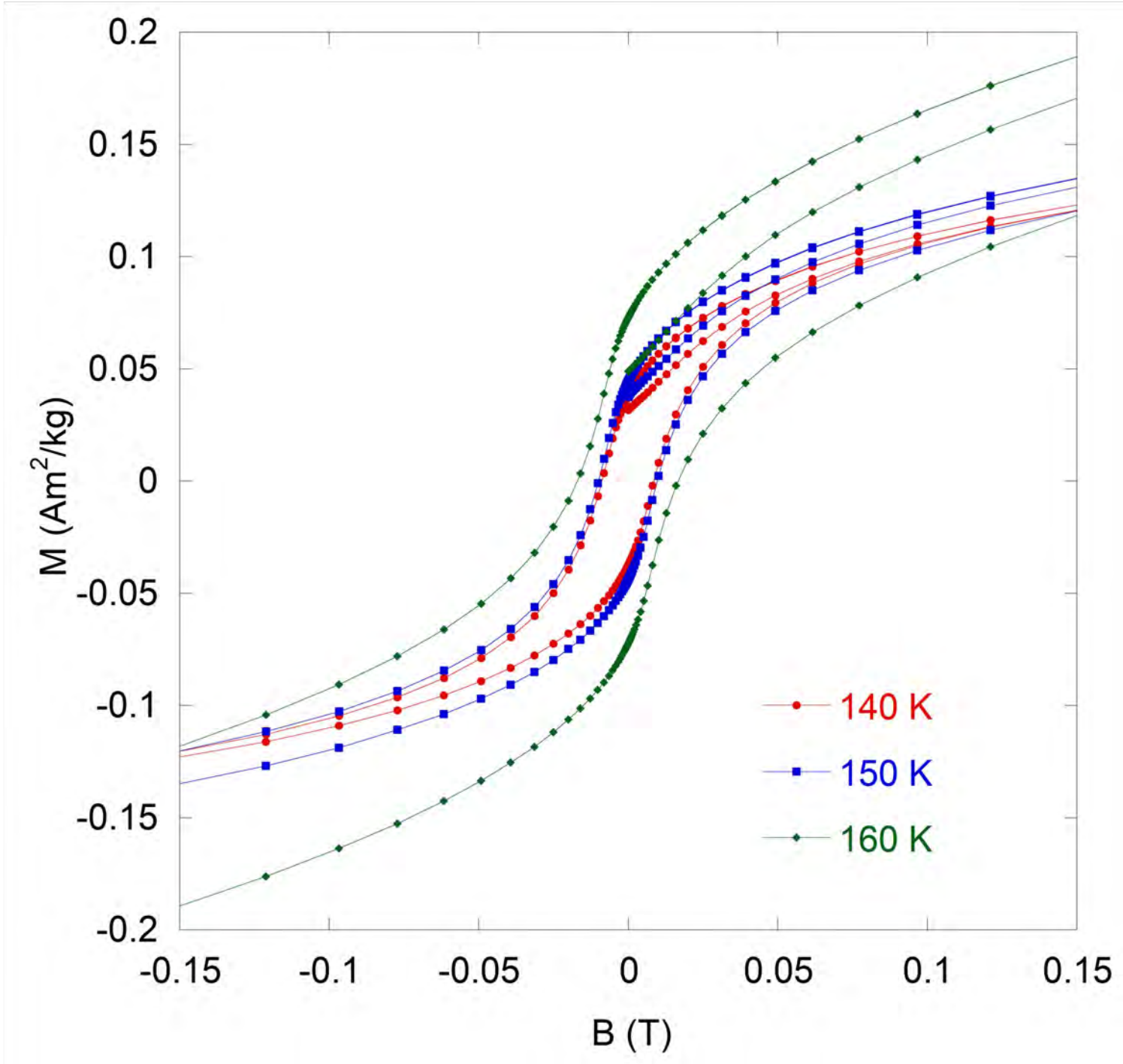
0.2
0.15
0.1
0.05
0
-0.05
-0.1
-0.15
-0.2
M (Am²/kg)
-0.15
-0.1
-0.05
0
0.05
0.1
0.15
B (T)
140 K
150 K
160 K

c)

Figure 6

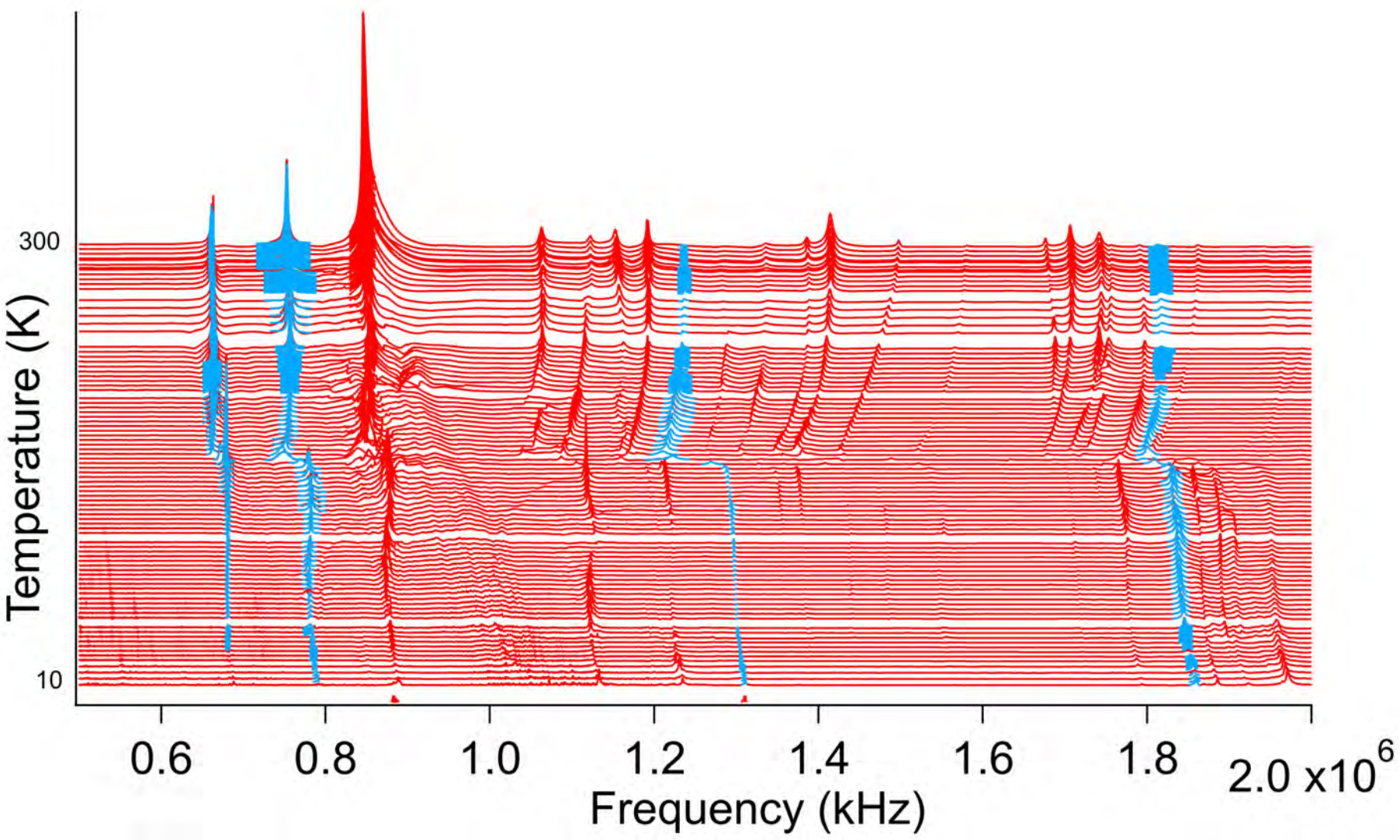

Figure 7a

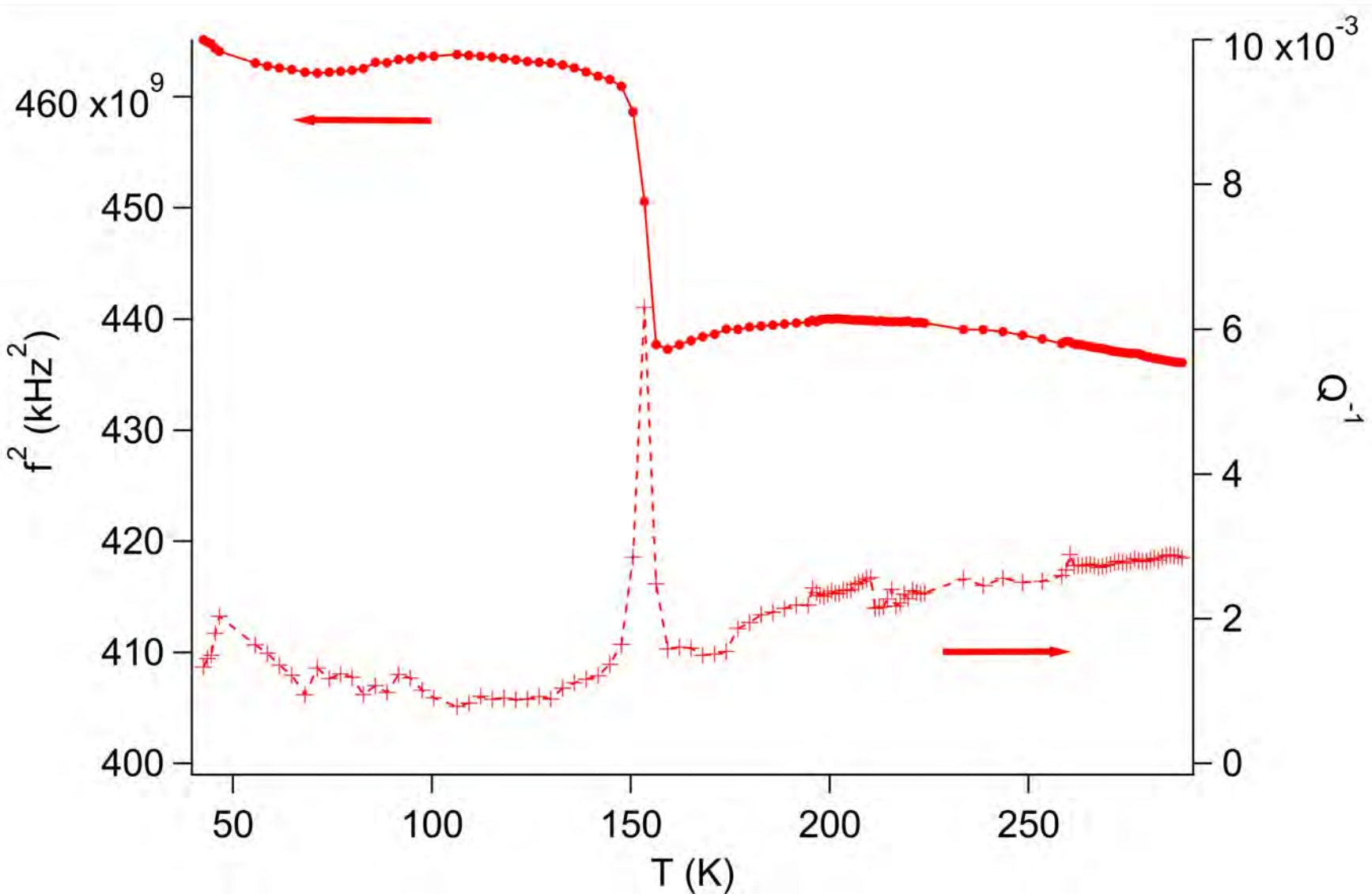
460 x10^9
450
440
430
420
410
400
f^2 (kHz^2)
10 x10^-3
8
6
4
2
0
Q^-1
50
100
150
200
250
T (K)

a)

Figure 7b

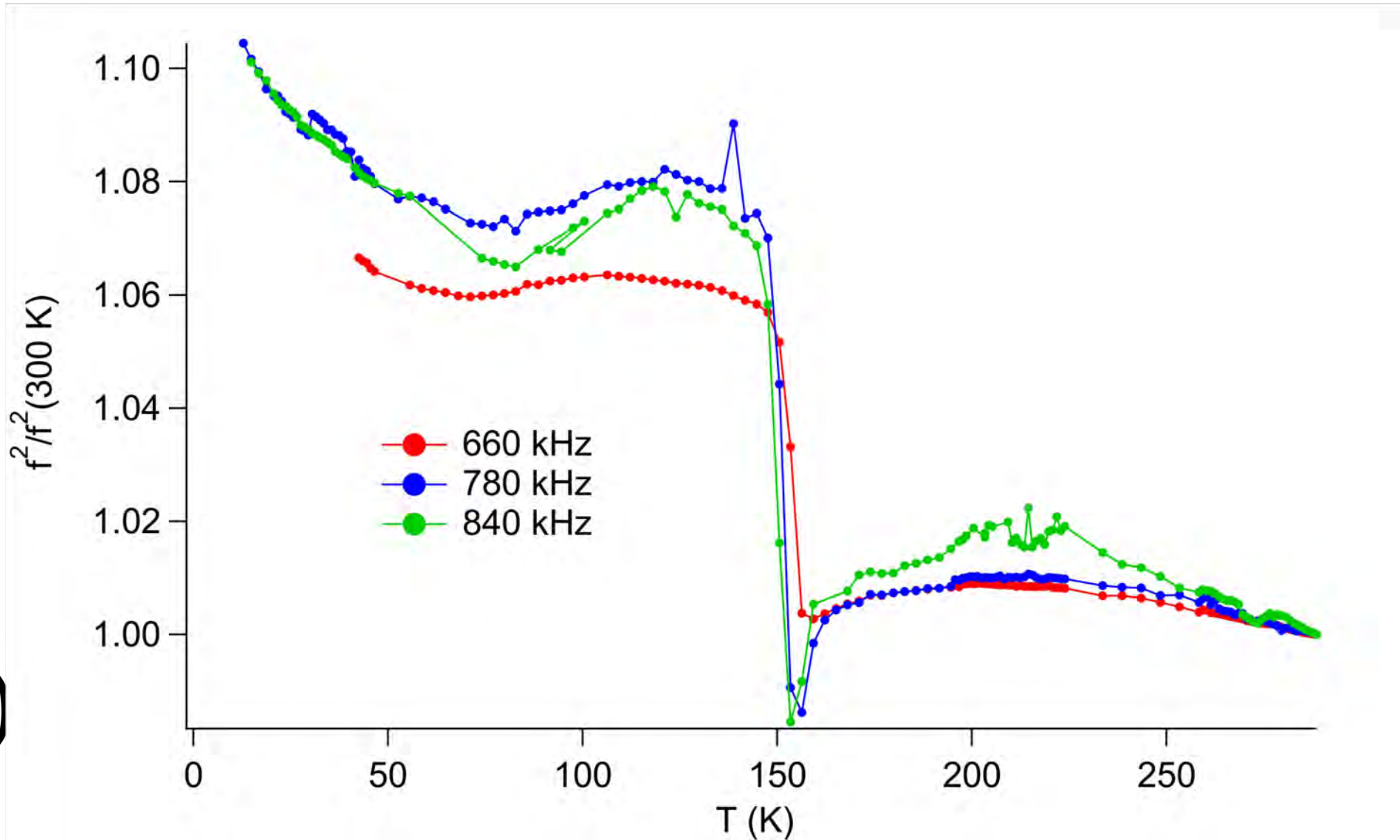
1.10
1.08
1.06
1.04
1.02
1.00
$f^2/f^2(300\ K)$
660 kHz
780 kHz
840 kHz
0
50
100
150
200
250
T (K)

b)

Figure 7c

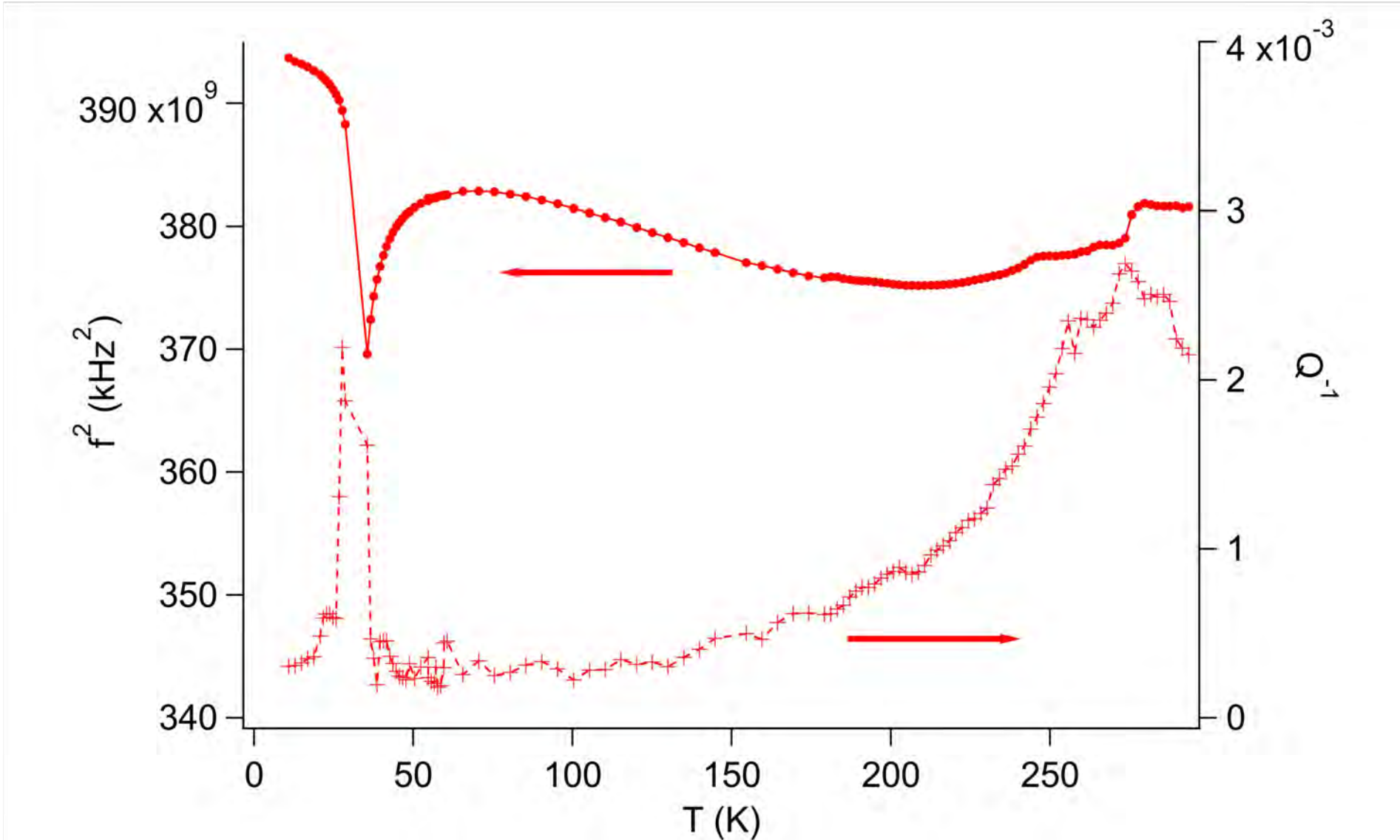
390 x10^9
380
370
360
350
340
f^2 (kHz^2)
4 x10^-3
3
2
1
0
Q^-1
0
50
100
150
200
250
T (K)

c)